4. B. Yaakobi, J. Delettrez, L. M. Goldman, R. L. McCrory, R. Marjoribanks, M. C. Richardson, D. Shvarts, S. Skupsky, J. M. Soures, C. Verdon, D. M. Villeneuve, T. Boehly, R. Hutchinson, and S. Letzring, *Phys. Fluids* **27**, 516 (1984).
5. A. Hauer *et al., Phys. Rev. Lett.* **53**, 2563 (1984).
6. B. Yaakobi, O. Barnouin, J. Delettrez, L. M. Goldman, R. Marjoribanks, R. L. McCrory, M. C. Richardson, and J. M. Soures, *J. Appl. Phys.* **57**, 4354 (1985).
7. R. C. Malone, R. L. McCrory, and R. L. Morse, *Phys. Rev. Lett.* **34**, 721 (1975).
8. Earlier versions of *LILAC* are described in LLE Reports No. 16 and No. 36 (1976).
9. B. L. Henke, H. T. Yamada, and T. J. Tanaka, *Rev. Sci. Instrum.* **54**, 1311 (1983).
10. B. L. Henke and P. A. Jaanimagi, to be published in *Rev. Sci. Instrum.*
11. M. C. Richardson, S. Skupsky, J. M. Soures, W. Lampeter, S. Tomer, R. Hutchison, M. Dunn, and W. Beich, Conference on Lasers and Electro-optics, Technical Digest, paper FK3 (1984).
12. S. Skupsky (private communication).
13. S. E. Bodner, *J. Fusion Energy* 1, 221 (1981).

2.B Short-Wavelength, Single-Shell, Direct-Drive Pellet Designs

The response of direct-drive targets to irradiation nonuniformity has been investigated for reactor-size targets with laser-driver energies between 1 MJ and 10 MJ. One-dimensional hydrodynamics calculations were performed to examine the scaling of energy production for targets consistent with specific constraints on aspect ratio (for hydrodynamic stability) and on peak laser irradiation (to minimize plasma instabilities). Two-dimensional hydrodynamic simulations were performed to investigate the effects on target performance produced by irradiation nonuniformities from the multiple overlapping laser beams. These calculations concentrated on the effects of the longer-wavelength nonuniformities (spherical harmonic modes $\ell \leq 8$) characteristic of energy imbalance between beams, beam mispointing, and nonideal beam shapes. Shorter-wavelength nonuniformities are presently under investigation; they can create shell deformations that will be amplified

substantially due to the Rayleigh-Taylor instability.[1-3] Constraints imposed by unstable growth have been applied in determining pellet designs with acceptable aspect ratios (shell radius divided by shell thickness). Generically, the targets considered for this study were single-shell pellets consisting of a low-Z ablator material (CH_2), a cryogenic DT fuel layer and an inner region of DT vapor determined by the initial temperature of the cryogenic fuel (Fig. 23.17). The laser irradiation was a shaped, KrF (250-nm) pulse in the energy range of 1–10 MJ (Fig. 23.18).

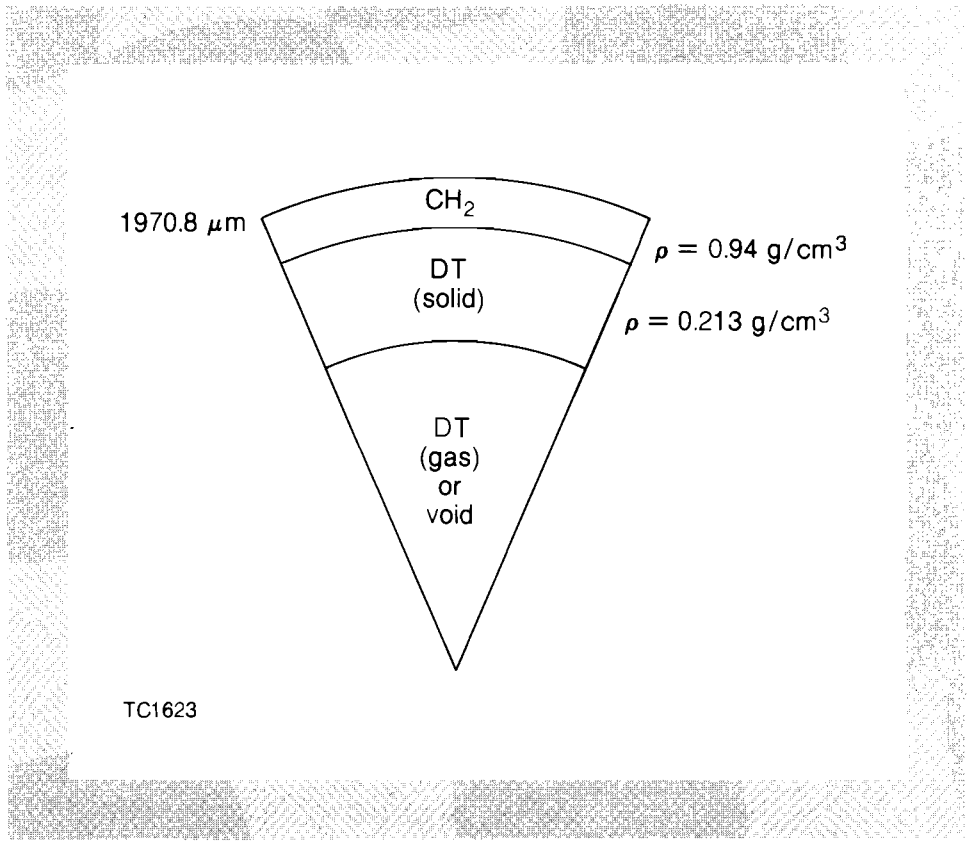

Fig. 23.17
1.6-MJ, single-shell target.

The issue of irradiation nonuniformity from multiple overlapping beams must be addressed for any direct-drive reactor system and pellet design study.[4-8] Typically, it is believed that variations in energy deposition on target should be less than ~1% rms[9,10] to prevent severe degradation of pellet performance due to shell deformation and subsequent core disruption. Simulations have shown that high irradiation uniformity can be obtained for direct-drive systems, using typical reactor focusing optics, by proper attention to the number and placement of individual beams[11] and by focusing each beam such that it initially irradiates approximately a complete hemisphere. (With the use of such highly non-normal laser irradiation a ray-trace algorithm[12] must be used to treat both the refraction of the incident laser light and deposition of laser energy in the plasma atmosphere. Changes in the critical-surface position and plasma-atmosphere size during the implosion result in changes in the illumination uniformity pattern, both in magnitude and shape, throughout the laser pulse.)

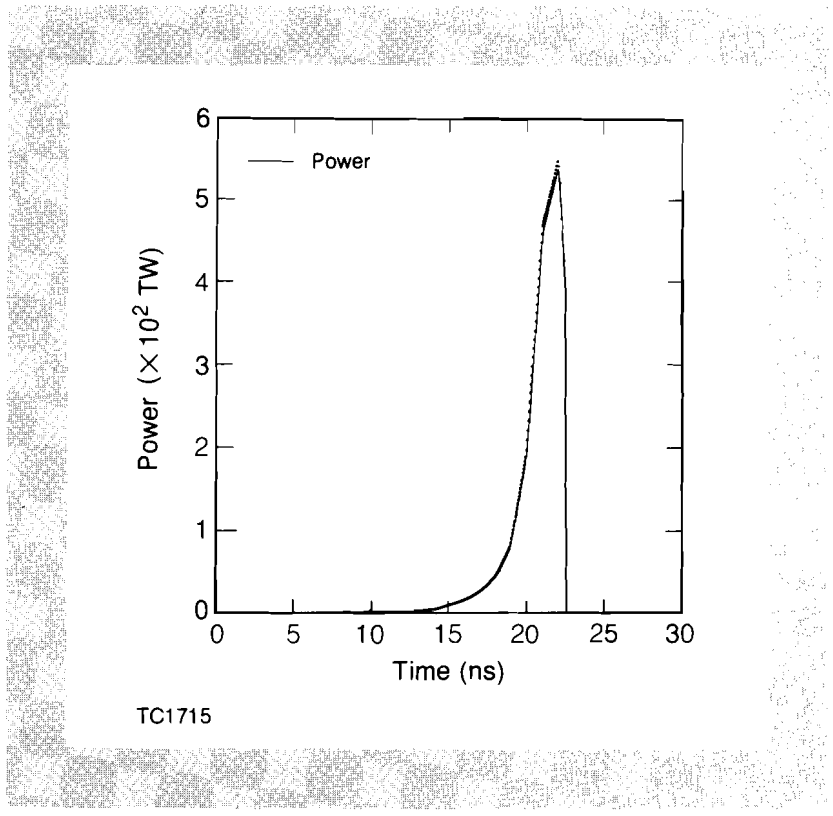

Fig. 23.18
Time-tailored laser pulse used for the 1.6-MJ design.

One-Dimensional Results

The 1-D pellet designs were carried out using the University of Rochester's hydrocode *LILAC*. *LILAC* contains Lagrangian hydrodynamics, tabular equation-of-state (SESAME[13]) thermonuclear burn, multigroup fusion product transport, and multifrequency-group radiation transport. The opacities used in the radiation transport calculation were obtained from reducing 2000 frequency group LTE LANL Astrophysical Library[14] tables to a desired group structure ($\sim$50 groups are used in most *LILAC* simulations). Laser deposition is done using a geometrical optics ray-trace[12] algorithm with energy deposition by inverse bremsstrahlung along each ray path. Flux limitation of electron thermal transport[15] is incorporated as a harmonic mean with the Spitzer-Härm electron thermal conductivity. [For all of the simulations presented in this report, the value of the flux limiter (f) was set to 0.04, with the maximum permitted heat flux given by $q_{max} = fn_e kT(kT/m_e)^{1/2}$.]

Some of the constraints imposed upon the designs are discussed below.

1. In-Flight Aspect Ratio

The in-flight aspect ratio is considered to be a measure of a target's ability to withstand shell breakup due to the Rayleigh-Taylor instability.[1-3,16] The definition[17] of the in-flight aspect ratio A(t) is given by $A(t) = \bar{R}(t)/\Delta R(t)$ where $\bar{R}(t)$ and $\Delta R(t)$ are a characteristic shell radius and thickness at time t. The value of $\Delta R(t)$ is found by first determining the radial location and value of the peak material density in the pellet. Next the radial locations are found both ahead and behind the peak

where the density is one e-folding below the maximum. The distance between the two locations defines $\Delta R(t)$, and $\bar{R}(t)$ is the average of the locations. One-dimensional simulations have shown that this definition accounts for ~75% of the imploding shell mass. This region represents the material that acts as the cold fuel layer and pusher surrounding the "spark-plug" region of the target. The effect of the Rayleigh-Taylor instability on the material identified by the above method is critical to target performance. The in-flight aspect ratio serves only as a guideline by which 1-D pellet designs can be judged as conservative or optimistic, until multidimensional calculations are available.

2. Convergence Ratio

Two convergence ratios have been considered in designing the single-shell pellets. The first is simply the initial radius of the DT fuel-pusher interface divided by the minimum radius obtained for that interface during the implosion. (If this interface is ablated during the implosion, we take the minimum radius to be that of the outermost unablated DT zone.) This definition serves as a measure of the approximate distance the ablator travels during the implosion and is used to estimate the number of possible e-foldings an infinitesimal perturbation would experience.

A second convergence ratio is defined to characterize the spark-plug region, which ignites the bulk of the thermonuclear fuel mass. Hydrodynamic simulations show that the spark plug for these pellets is primarily composed of the material from the initial low-density vapor region of the pellet. Thus, the spark-plug convergence ratio is defined as the initial radius of the interface between the gas and the cryogenic layer divided by the radial location of this interface at the time of ignition. The spark-plug convergence ratio is used in conjunction with the size of the spark-plug region at the time of ignition to estimate the possible effects of instability during the deceleration phase of the implosion.

3. Laser Irradiance

To prevent the generation of energetic electrons from plasma processes,[18,19] the peak laser irradiance was kept below a few times 10^{15} W/cm^2 at the critical surface. The peak irradiance levels were reached only near the end of the laser pulse. Since reactor-size plasma scale lengths have not yet been investigated in the laboratory, the possible effects of plasma phenomena at high laser intensities are not well understood.

4. Illumination Uniformity

Calculations[11] for direct-drive illumination uniformity have examined different laser configurations containing up to 96 beams. Typically, for all configurations considered, optimal uniformity is obtained at a focal distance ~ 0.9 times the distance for tangential focus (as measured from the target center). Tangential focus is defined as the focal position where a beam subtends an entire target hemisphere; it is at a distance of $2 \times f^{\#} \times R$, where $f^{\#}$ is the f-number of the final optical element and R is the target radius. As the target radius (or more correctly, the critical-density radius) decreases during the implosion, the amount of the target subtending each beam will change, resulting in a change in uniformity.

The strategy used here was to focus initially at the point of optimum uniformity. As focusing conditions deviate from optimum during the implosion, the irradiation nonuniformity will increase, but so will the size of the plasma atmosphere surrounding the target, permitting smoothing of some nonuniformities in energy deposition by thermal conduction. (For a system with more than ~ 60 beams, the increase in nonuniformity during the implosion was found to be relatively small). For all the 1-D designs considered here, f/20 optics was used in the ray-trace algorithm with the initial focal position at 36 times the target radius.

5. Target Fabrication

It must be noted that all of the pellet designs considered here are not consistent with current target fabrication technology. The large DT, gas-fill pressure that would exist at room temperature inside the ablator shell exceeds present fabrication limits. (Present technology is limited to approximately 100 atm, while targets considered here contain nearly 600 atm of DT at room temperature.)

A summary of the target design characteristics for targets at 1.6 MJ and 4.1 MJ is shown in Table 23.I. Both cases use the generic target and pulse shape of Figs. 23.17 and 23.18. (The 4.1-MJ design is a scaled-up version of the 1.6-MJ design—i.e., larger target and longer pulse.) The variation in pellet gains with incident laser energy for the single-shell, 1-D designs considered in this study is shown in Fig. 23.19. [The shaded band about the central line indicates the changes that were observed by varying the value of the flux limiter (f) between 0.03 and 0.06.] No attempt was made to adjust target parameters to optimize the gain when the flux limiter was changed. From Fig. 23.19 it can be

Table 23.I
Target design characteristics and results.

Target Design Characteristics and Results

	1.6 MJ	4.1 MJ
Energy Supplied	1.57 MJ	4.09 MJ
Energy Absorbed	1.26 MJ	3.51 MJ
Absorption Fraction	0.80	0.86
Peak Laser Intensity	1.1×10^{15} W/cm^2	1.8×10^{15} W/cm^2
Peak Laser Power	600 TW	800 TW
Hydrodynamic Efficiency	10%	10%
Peak Fuel Mass-Averaged Implosion Velocity	35.0 cm/μs	30.0 cm/μs
Peak Fuel $<\rho R>$	2.56 g/cm^2	4.0 g/cm^2
Convergence Ratio	13.8	10.7
Convergence Ratio (spark plug)	70.0	80.0
In-Flight Aspect Ratio	80.0	65.0
Gain (Total TN Products)	68.0	120.0

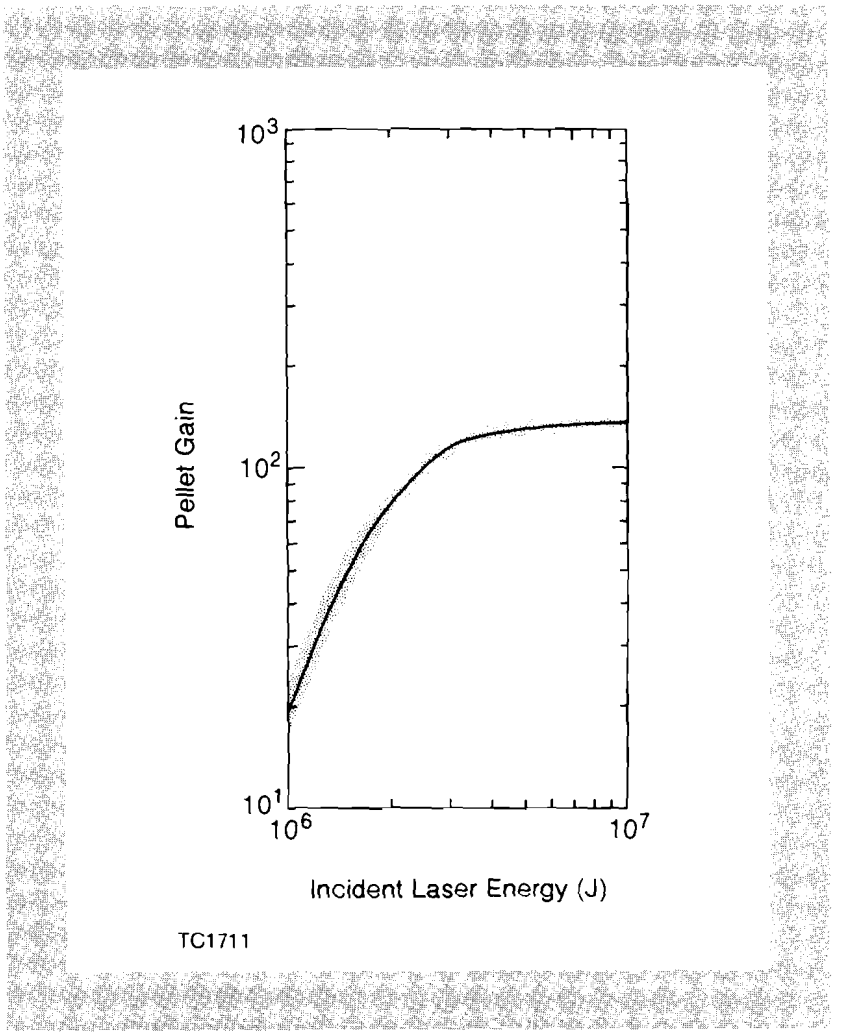

Fig. 23.19
Energy gain versus incident KrF laser energy for single-shell, direct-drive pellet designs.

seen that the pellet gain levels off to ~120 for incident energies above ~4.0 MJ.

In order to estimate the effect of mixing between the plastic pusher and the igniting DT during shell deceleration and burn, we have applied a free-fall argument. By extrapolating the trajectory of the plastic fuel interface to 80% of the minimum fuel core radius, a time is estimated that corresponds to the time at which half the fuel mass would be mixed with ablator material. Thermonuclear (TN) yield that would accrue after this time is ignored in the calculation. The result of this estimate is that 98% of the TN yield is released before the plastic mixes with half the fuel mass. This may, however, still overestimate the yield. Pellets of this generic type (i.e., a large thickness of cryogenic DT and a thin ablator layer) effectively use the outer region of the fuel as the pusher during final core assembly. Most, if not all, of the plastic has been ablated once the burn has begun. Therefore, the more important questions with respect to mixing and possible TN yield reduction for these pellets are (1) the unknown effects of cold DT mixing with hot DT during the spark-plug formation, and (2) bulk mixing of DT and its effect on pellet performance once the burn wave has begun to propagate outward from the spark region.

Two-Dimensional Results

The above results have assumed uniform laser irradiation. For multiple beam overlap, there will be some nonuniformities in irradiation. If large enough, they can lead to a distorted compressed core and a reduced target gain. The effects of long-wavelength nonuniformities (ℓ = 2,4,8) have been calculated for the 1.6-MJ design. Modes ℓ = 2 and ℓ = 4 are generally produced by beam energy imbalance and beam mispointing. The ℓ = 8 mode is characteristic of the nonuniformity produced in beam overlap by 24–32 beams (even assuming perfectly smooth laser profiles).[4] Nonuniformities in temperature produced by these long-wavelength modes are not expected to be significantly attenuated by thermal smoothing within the target atmosphere and, therefore, will distort the target drive during the entire time of irradiation. Shorter-wavelength nonuniformities can be smoothed by thermal conduction once an adequate plasma atmosphere has been established. However, the distortion produced prior to that time will continue to grow exponentially during acceleration and deceleration of the target shell due to the Rayleigh-Taylor instability.

The effects of nonuniformities were examined using the University of Rochester's 2-D (R-Z) Lagrangian hydrodynamics code *ORCHID*. The laser nonuniformity was applied as a single Legendre mode (ℓ) with varying amplitudes: peak-to-valley amplitudes of 2% and 4% for the ℓ = 2 and 4 cases, and amplitudes of 1% and 2% peak to valley for the ℓ = 8 case.

Characteristic results are presented here for an ℓ = 4 nonuniformity, imposed with peak irradiation on the pole (Z-axis). The time history of the spark-plug formation, ignition, and subsequent burn for the 2% peak-to-valley (σ_{rms} = 0.65%) case is shown in Figs. 23.20 through 23.22. Figure 23.20 displays density contours in g/cm^3; Fig. 23.21 shows ion temperature contours in eV; and Fig. 23.22 displays the velocity vectors showing the fluid motion at four different times. The spark-plug region is forming in the two upper frames of all three figures. In the upper right-hand frame of Fig. 23.22, the material that was initially in the cryogenic DT layer has ignited as indicated by the region of rapidly diverging velocity vectors.

Ignition and thermonuclear burn in these targets proceeds in the following manner. As the implosion reaches the core-assembly phase, the ion temperature in the gas begins to rise due to both PdV work and shock heating. The particles emitted from the gas region initially begin to deposit energy throughout the main fuel layer due to the low $<\rho R>$ at this time. As the main fuel body continues to implode, a point is reached where the $<\rho R>$ rises to values large enough to stop most of the α particles within a short distance into this region. This is the point we refer to as ignition for the pellet designs identified in this study. The ion temperature and $<\rho R>$ in the gas region at this time are of the order of 10 keV and ~0.1 g/cm^2, respectively. In the region where most of the α particles are stopped, the ion temperature is ~2.75 keV while the $<\rho R>$ is ~0.55 g/cm^2 as measured from the target center.

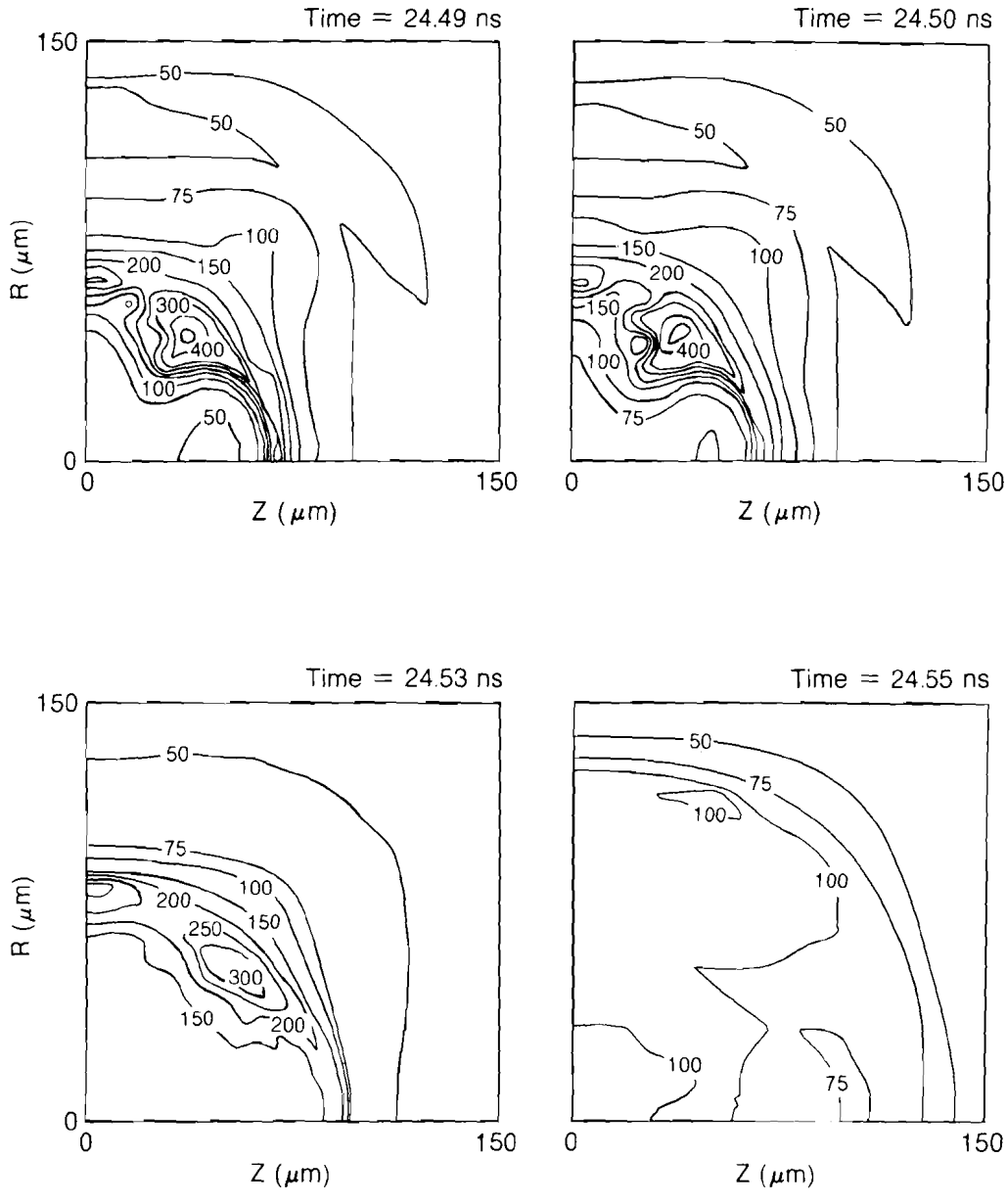

TC1701

Fig. 23.20
Density contours (g/cm^3) at various times for the ℓ = 4, 2% peak-to-valley, 1.6-MJ implosion.

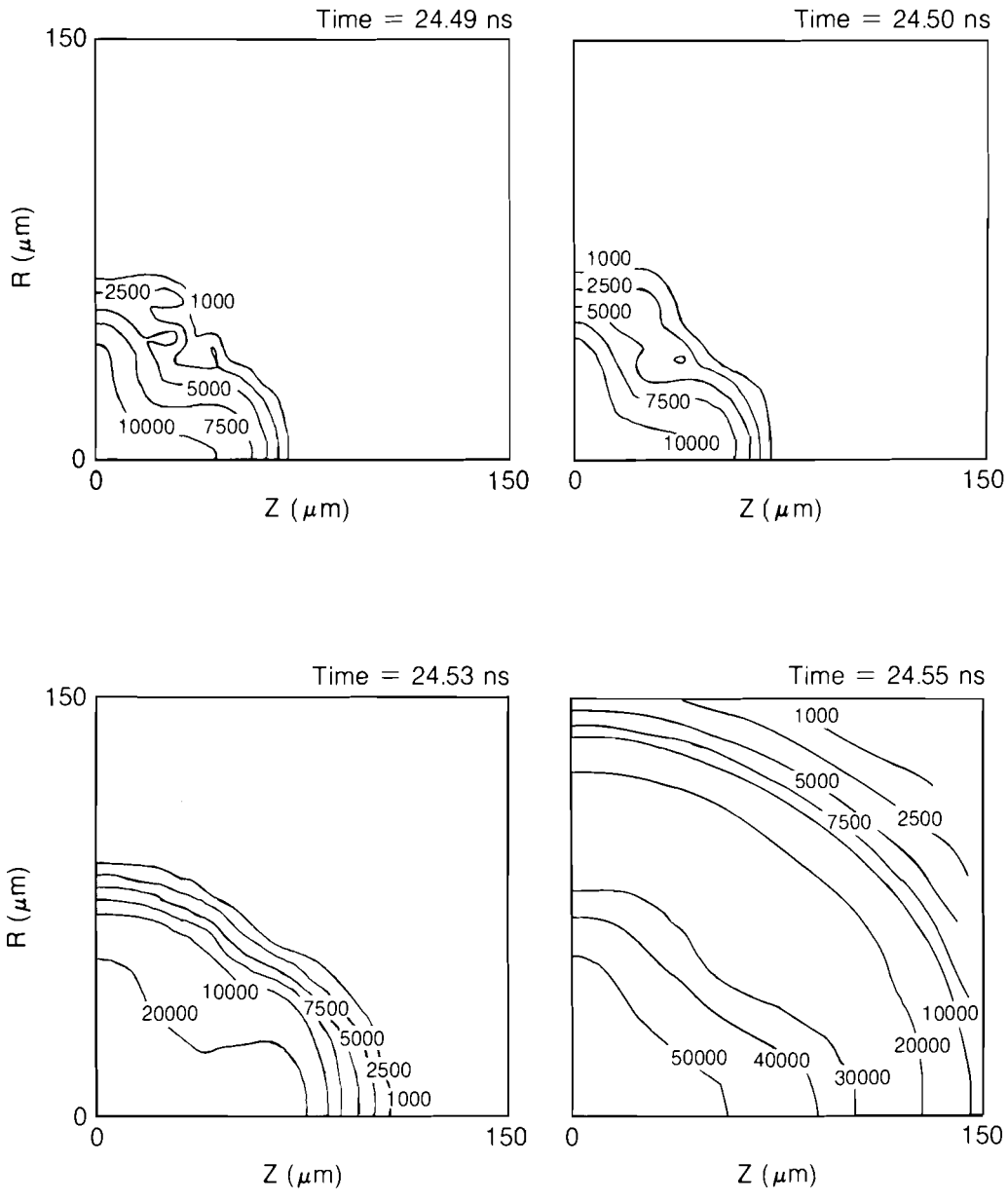

Fig. 23.21
Ion temperature contours (eV) at various times for the ℓ = 4, 2% peak-to-valley, 1.6-MJ implosion.

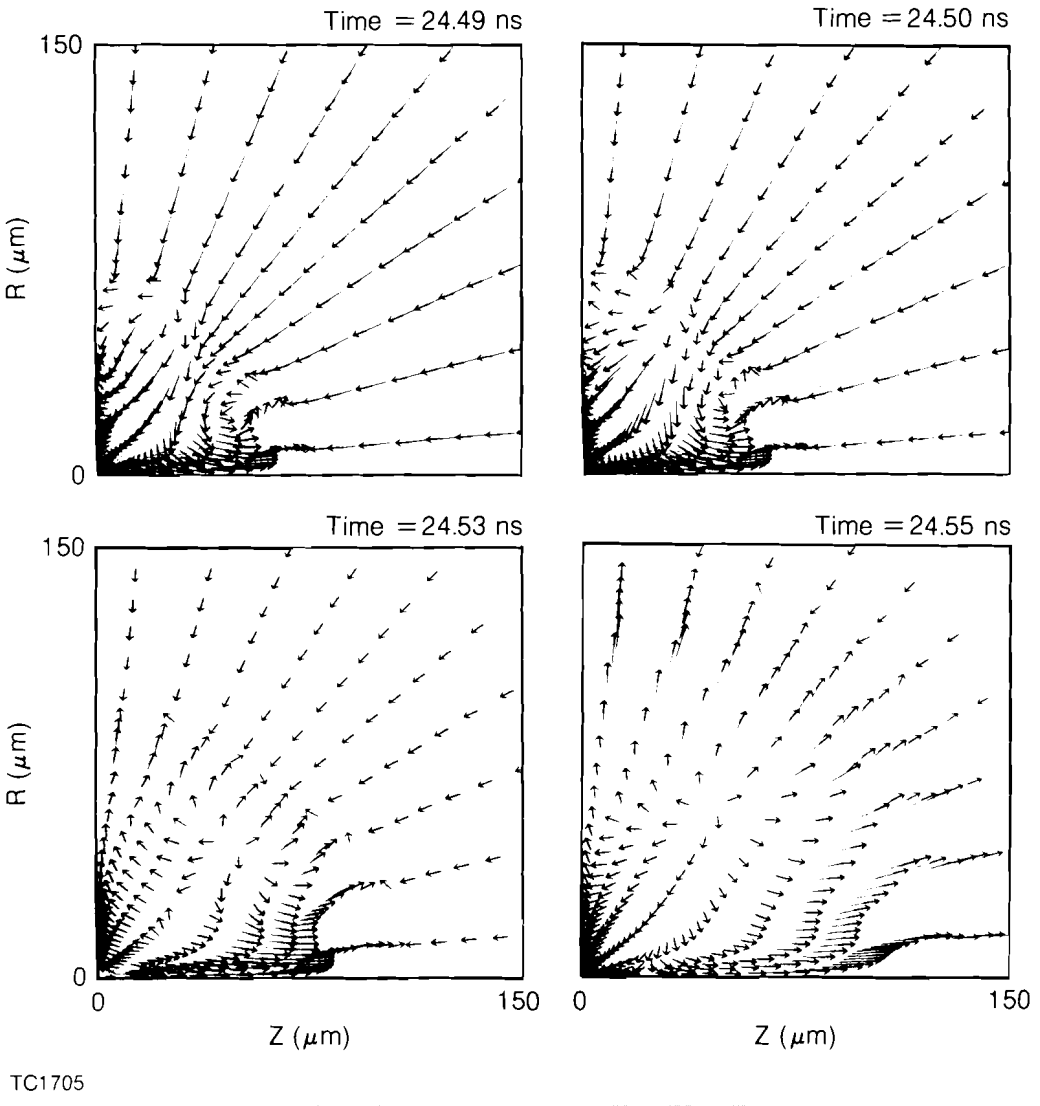

Fig. 23.22
Velocity vectors at various times for the ℓ = 4, 2% peak-to-valley, 1.6-MJ implosion.

At the time of core assembly and burn, the $<\rho R>$ of the core was found to be reversed in phase from the applied illumination perturbation. Figure 23.23 displays $<\rho R>$ versus polar angle (Z axis equals 0.0°). The left-hand frame of Fig. 23.23 shows the $<\rho R>$ before final core assembly. Note that the $<\rho R>$ phase is that of the applied illumination. The middle frame shows that the phase of the $<\rho R>$ is beginning to change as the spark plug is forming, and the right-hand frame is at the time near peak $<\rho R>$ where the reversal in the applied perturbation amplitude is clearly evident. This reversal begins before the shell

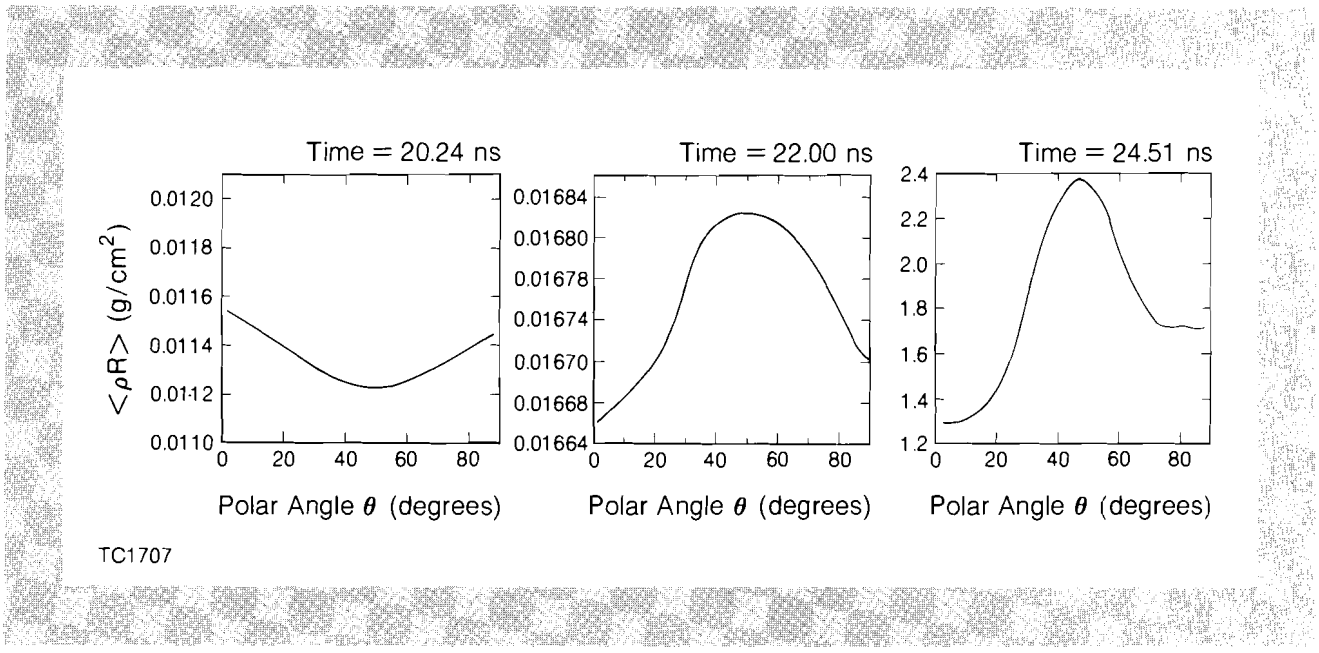

Fig. 23.23
Fuel <ρR> (g/cm²) versus polar angle at various times for the ℓ = 4, 2% peak-to-valley, 1.6-MJ implosion.

decelerates and is due to an azimuthal pressure generated by the convergence of the distorted shell. During deceleration, a combination of jetting due to the azimuthal pressure generation and Rayleigh-Taylor unstable growth is responsible for the development of the perturbation near the interface between the gas and cryogenic DT layers seen in Fig. 23.20. The temperature profiles during the core assembly phase also follow the density perturbation early in time (upper two frames, Fig. 23.21). However, once the pellet ignites, the combination of α-particle energy deposition and thermal transport acts to smooth variations in the temperature profiles in the pellet core resulting in a relatively radially propagating burn front.

A summary of the growth of the deformation is shown in Fig. 23.24. Plotted is the maximum-minus-minimum radial location ($\Delta R_{max\text{-}min}$) of the Lagrangian interface between the gas region and the cryogenic DT layer versus the average radius ($\bar{R}$) of that interface, for the ℓ = 4, 4% peak-to-valley case. When the average interface location reaches 150 μm, the phase of the perturbation begins to change, resulting in a reduction of $\Delta R_{max\text{-}min}$. However, below ~75 μm, the perturbation amplitude of this surface grows rapidly, until ($\Delta R_{max\text{-}min}/\bar{R}$) is of the order of unity (see Fig. 23.25).

The 2%, ℓ = 4 nonuniformity caused an 8% reduction in target gain. When the illumination perturbation amplitude was increased to 4% peak to valley (σ_{rms} = 1.25%), the pellet failed to ignite. The increased perturbation caused a large quantity of colder DT to be forced into the spark-plug region, thereby (1) cooling the spark plug by conduction and (2) converting its internal energy into kinetic energy as it moved out of the way of the incoming colder fuel. This can be seen in Fig. 23.25, which shows a comparison of the ℓ = 4, 2% and 4% peak-to-valley cases at the time of ignition. (The shaded regions on the grid plots represent the initial low-density fill-gas material.) The larger disruption of the spark-plug region is clearly evident for the 4% peak-to-valley case.

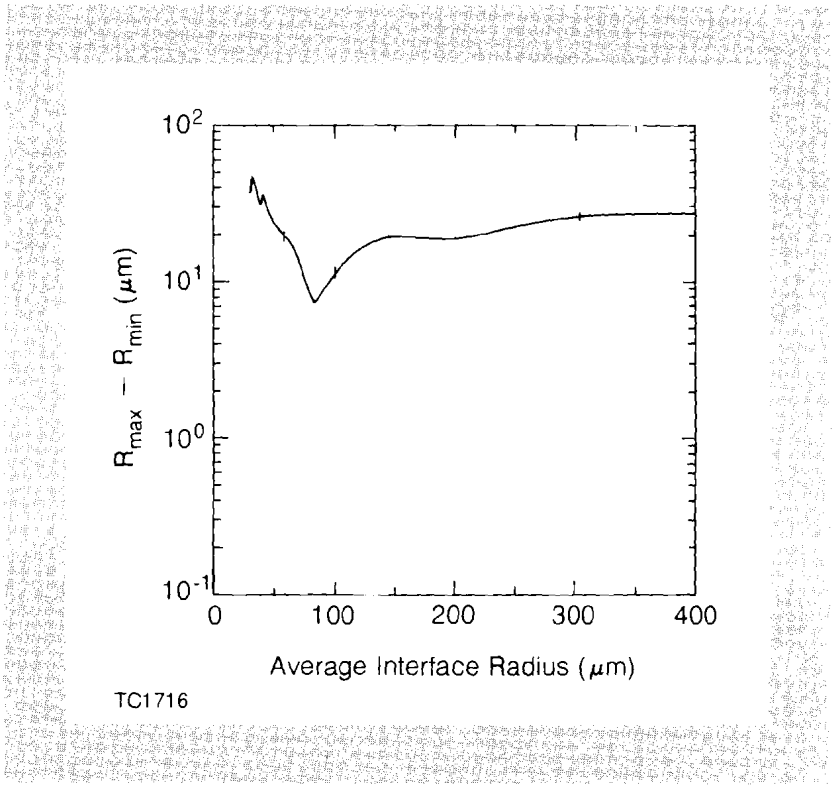

Fig. 23.24
Maximum-minus-minimum radius of the gas-solid interface versus radius for the $\ell = 4$, 4% peak-to-valley case.

A summary of the degradation in target gain with increased irradiation nonuniformity is shown in Fig. 23.26 for the three modes considered. This amount of degradation is not a general result for direct-drive targets, but represents the performance of only a single design. In particular, analysis of the failure of the 4%, $\ell = 4$ case suggests that a substantial target gain would have occurred for a small increase in laser energy. The general trend is that the shorter modes are the most dangerous, and that any thermal smoothing of the nonuniformity that might have occurred is compensated for by Rayleigh-Taylor growth in the target.

Future Work

One possible method of reducing the sensitivity of these types of pellets to irradiation nonuniformities would be to decrease the spark-plug convergence ratio. As an example, Fig. 23.27 displays the spark-plug convergence ratio and pellet-gain versus the DT gas density (which is determined by the DT-layer initial temperature) for the 1.6-MJ design. Note that the spark-plug convergence ratio can be halved without reducing the pellet gain for this design. The response to irradiation nonuniformities of targets with the lower spark-plug convergence ratio is presently under investigation.

A second area requiring further examination is the effect of the Rayleigh-Taylor instability on imploding shells. Due to resolution limitations, such simulations will have to be performed using "conical" sections, with a slip surface between $\theta = 0°$ and 90°. These runs cannot be taken to final core implosion due to incorrect boundary conditions about the slip surface. However, these simulations will

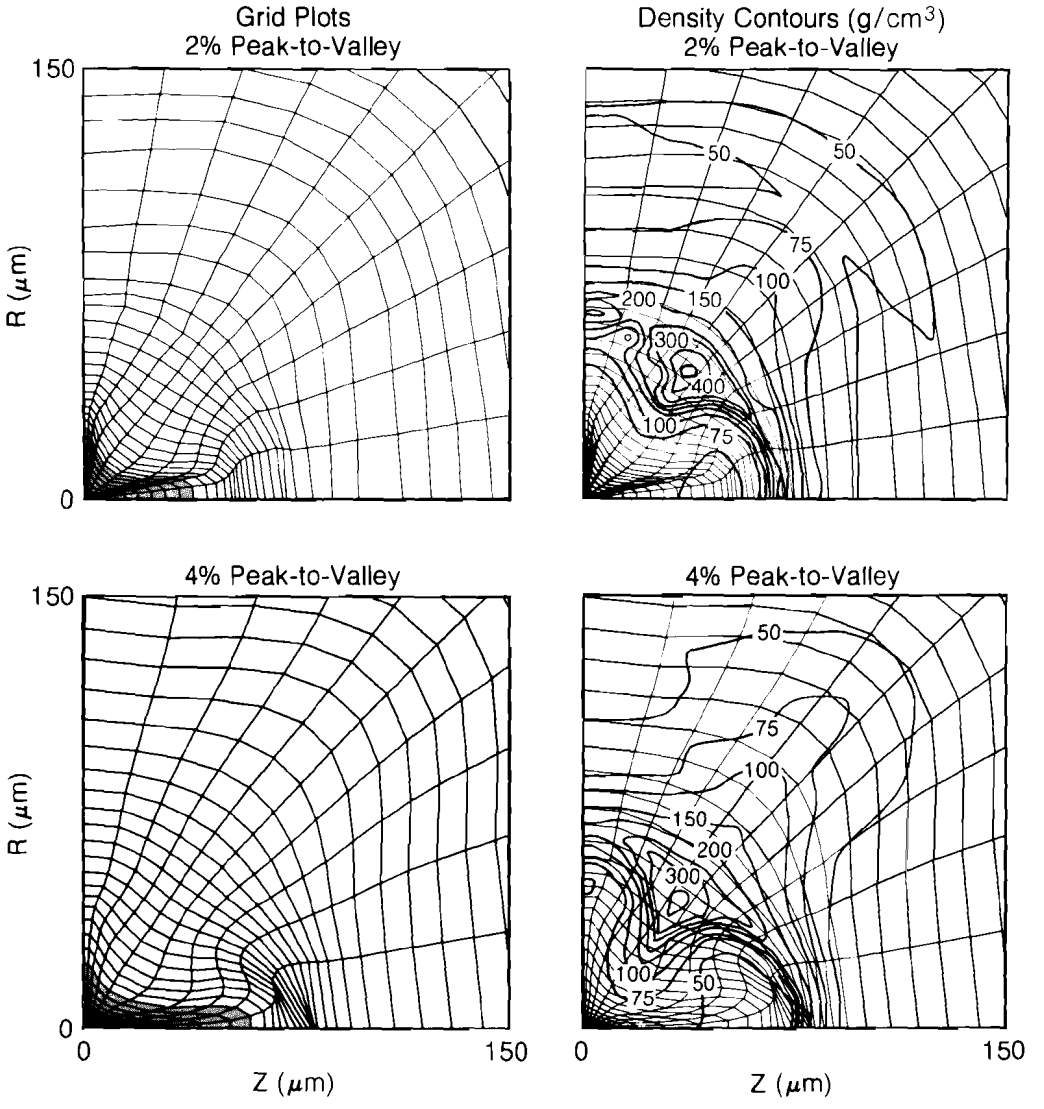

Fig. 23.25
Spark-plug region at the time of "ignition" for two $\ell = 4$ cases: one with a 2% peak-to-valley imposed irradiation nonuniformity and the other with a 4% nonuniformity.

address the effects of short-wavelength Rayleigh-Taylor unstable growth on the shell (pusher) during the rapid acceleration phase of the implosion, before the effects of spherical convergence become important. These studies will also help to determine more accurate hydrodynamic limitations, which will be used in the examination of 1-D pellet designs.

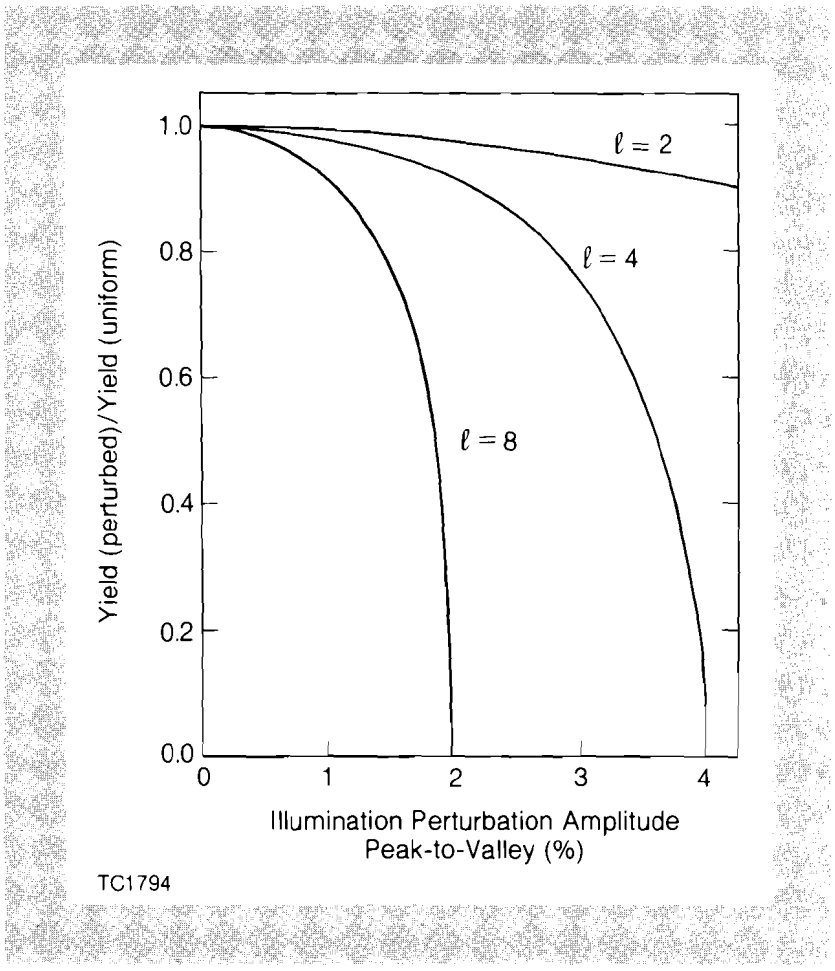

Fig. 23.26
Yield reduction versus illumination perturbation for the 1.6-MJ pellet designs.

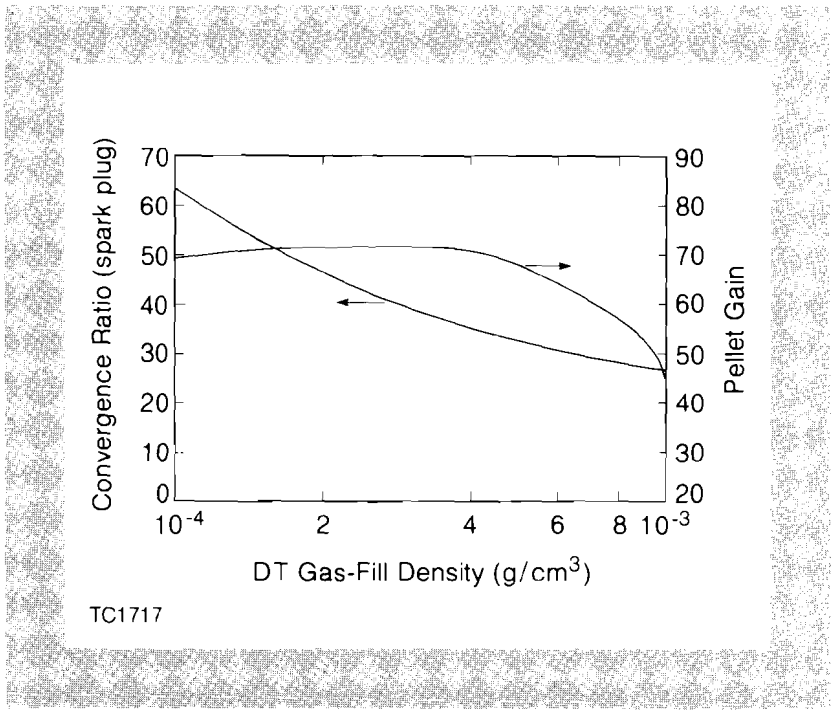

Fig. 23.27
Pellet convergence ratio and pellet gain at the time of ignition versus DT gas-fill density for 1.6-MJ pellet designs.

Work is also under way to examine methods of reducing the in-flight aspect ratios of the 1-D designs identified in this study. A reduction in the in-flight aspect ratio will be beneficial when considering the effects of short-wavelength, Rayleigh-Taylor unstable growth. However, even with reductions in the in-flight aspect ratio, the effects of long-wavelength perturbations of the order of $\ell \leq 12$ will still be important. Their "feed-through" to the inner surface of the shell will not be greatly reduced by decreases in the in-flight aspect ratio; their effect on the final core assembly and pellet performance may remain essentially unchanged even if the in-flight aspect ratio is reduced by factors of 2.

ACKNOWLEDGMENT

This work was supported by the U.S. Department of Energy Office of Inertial Fusion under agreement number DE-FC08-85DP40200, by the Los Alamos National Laboratory under contract number 9-X54-H8413-1, and by the Laser Fusion Feasibility Project at the Laboratory for Laser Energetics, which has the following sponsors: Empire State Electric Energy Research Corporation, General Electric Company, New York State Energy Research and Development Authority, Northeast Utilities Service Company, Ontario Hydro, Southern California Edison Company, The Standard Oil Company, and University of Rochester. Such support does not imply endorsement of the content by any of the above parties.

REFERENCES

1. G. S. Fraley, W. P. Gula, D. B. Henderson, R. L. McCrory, R. C. Malone, R. J. Mason, and R. L. Morse, in *Plasma Physics and Controlled Nuclear Fusion Research, Tokyo, Japan* (International Atomic Energy Agency, Vienna, 1974), Vol. 2, p. 543.
2. C. P. Verdon, R. L. McCrory, R. L. Morse, G. R. Baker, D. I. Meiron, and S. A. Orszag, *Phys. Fluids* **25**, 1653 (1982).
3. W. C. Mead and J. D. Lindl, LLNL Report UCRL-78457 (1976).
4. S. Skupsky and K. Lee, *J. Appl. Phys.* **54**, 3662 (1983).
5. Lawrence Livermore Laboratory Laser Program Annual Report UCRL-50021-74, p. 219 (1975).
6. J. E. Howard, *Appl. Opt.* **16**, 2764 (1977).
7. A. J. Scannapieco and H. Brysk, *J. Appl. Phys.* **50**, 5142 (1979).
8. K. Lee, R. L. McCrory, and R. Hopkins, Laboratory for Laser Energetics Report No. 88 (1981).
9. S. E. Bodner, *J. Fusion Energy* **1**, 221 (1981).
10. S. Skupsky, R. L. McCrory, R. S. Craxton, J. Delettrez, R. Epstein, K. Lee, and C. Verdon, in *Laser Interaction and Related Plasma Phenomena*, edited by H. Hora and G. H. Miley (Plenum, New York, 1984), Vol. 6, p. 751.
11. LLE Review **19**, 120 (1984).
12. M. Born and E. Wolf, *Principles of Optics* (Pergamon, New York, 1975), p. 123.
13. B. I. Bennett, J. D. Johnson, G. I. Kerley, and G. T. Rood, Los Alamos National Laboratory Report LA-7130 (1978).